Molecular Dynamics and Structural Studies of Zinc Chloroquine Complexes

Mirko Paulikat[a,‡], Daniele Vitone[b,‡], Florian K. Schackert[a,c,‡], Nils Schuth[d,‡], Alessandra Barbanente[b], GiovanniMaria Piccini[e], Emiliano Ippoliti[a], Giulia Rossetti[a,f,g], Adam H. Clark[h], Maarten Nachtegaal[h], Michael Haumann[i], Holger Dau[i], Paolo Carloni[a,c,*], Silvano Geremia[j], Rita De Zorzi[j], Liliana Quintanar[d,*], Fabio Arnesano[b,*]

[a] *Computational Biomedicine (IAS-5/INM-9), Forschungszentrum Jülich GmbH, 52428 Jülich, Germany*

[b] *Department of Chemistry, University of Bari "Aldo Moro", 70125 Bari, Italy*

[c] *Department of Physics, RWTH Aachen University, 52062 Aachen, Germany*

[d] *Department of Chemistry, Center for Research and Advanced Studies (Cinvestav), 07480 Mexico City, Mexico*

[e] *Euler Institute, Università della Svizzera italiana, 6962 Lugano, Switzerland*

[f] *Jülich Supercomputing Centre (JSC), Forschungszentrum Jülich GmbH, 52428 Jülich, Germany*

[g] *Department of Neurology, RWTH Aachen University, 52062 Aachen, Germany*

[h] *Paul Scherrer Institute, 5232 Villigen, Switzerland*

[i] *Department of Physics, Freie Universität Berlin, 14195 Berlin, Germany*

[j] *Department of Chemical and Pharmaceutical Sciences, University of Trieste, 34127 Trieste, Italy*

ABSTRACT: Chloroquine (CQ) is a first-choice drug against malaria and autoimmune diseases. It may act as a zinc ionophore. In this study, state-of-the-art computations and experiments were leveraged to solve the structure of the Zn chloride-CQ complex in solution and in solid state. The integration of different techniques (NMR, ESI-MS, X-ray absorption and diffraction methods) together with *ab initio* molecular dynamics simulations, overcomes the issues related to the kinetic lability of zinc complexes. Within the physiological pH range, CQ binds Zn^{2+} through the quinoline ring nitrogen, forming $[Zn(CQH)Cl_x(H_2O)_{3-x}]^{(3+)-x}$ (x = 0, 1, 2, 3) tetrahedral complexes. The $Zn(CQH)Cl_3$ species is stable at neutral pH and at high chloride concentrations typical of the extracellular medium, but metal coordination is lost at moderately low pH, suggesting the release of Zn^{2+} ions into the lysosomal lumen. $[Zn(CQH)(H_2O)_4]^{3+}$ may exist in the absence of chloride. This *in vitro* / *in silico* approach can be extended to other metal-targeting drugs and and bioinorganic systems.

INTRODUCTION

Chloroquine (CQ) is a first-choice drug against malaria and autoimmune diseases, such as lupus erythematosus and rheumatoid arthritis.[1] It has recently been used for the emergency treatment of COVID-19.[2] In parasite digestive vacuoles, the pH is approximately 5.2.[3] At this pH, the 4-aminoquinoline moiety is protonated (doubly positively charged) and undergoes trapping in these lysosome-related acidic organelles.[4,5] The lysosomal targeting (lysosomotropism) of CQ is not only responsible of its antimalarial properties;[6] indeed, the endosomal alkalinization can lead to inhibition of viral replication and infection.[7] Furthermore, the accumulation of CQ in acidic organelles can lead to the dysfunction of several enzymes required for proteolytic processing and post-translational modification of viral proteins.[8]

CQ has also been proposed to act as a zinc ion ionophore, i.e. a molecule capable of promoting Zn^{2+} cellular uptake.[9] This property of CQ has sparked interest because Zn^{2+} also accumulates in lysosomes and has antiviral properties through the inhibition of the viral enzyme RNA-dependent RNA Polymerase (RdRP) *in vitro*. Thus, Zn^{2+} ionophores block the replication of RNA viruses in cell cultures.[10] Zn^{2+} ions play an important role in the activation and function of immune cells and are associated with specific immune responses to bacteria, parasites and viruses.[11] For this reason, the combination of CQ with Zn^{2+} to treat SARS-CoV-2 infection, but the mechanism of action is still unclear and the risk/benefit ratio has proved too high to consider this drug safe and effective.[2,12–14]

Based on the proposed role of CQ, we deemed it of importance to investigate the coordination chemistry of this drug with the aim of obtaining mechanistic insights into the impact of CQ on Zn^{2+} binding and intracellular distribution.

Previous results by Navarro *et al.*[15,16] indicate that CQ in its diphosphate form (CQDP) can bind Zn^{2+} through different N donor atoms. The authors reported the synthesis of Zn-CQ complexes starting from chloride and acetate Zn^{2+} salts; in particular, for the former salt, they indicated the formation of a pentacoordinate $[ZnCl_2(CQ)(H_2O)_2]$ complex on the basis of the CHN elemental analysis.

To go beyond the limitations of a single structural characterization technique, an integrated approach is highly desirable. This is particularly useful in the case of zinc complexes (d^{10} electronic configuration), which are highly labile and variable in their coordination because of the lack of ligand field stabilization. This allows for dynamic coordination environments of zinc ions, which adopt different coordination numbers (from four to six) in interactions with substrates. Free zinc in aqueous solution is known to be hexa-coordinated, exchanging water molecules with a rate of ~0.05 ns^{-1}.[17] In proteins, zinc ions are commonly tetrahedral coordinated by O-, N- or S- atoms from glutamate/aspartate/water, histidine or cysteine residues. Instead, chlorido ligands can replace water molecules in zinc-aquo complexes to form a series of species from $[ZnCl_x(H_2O)_{6-x}]^{(2+)-x}$ up to $ZnCl_4^{2-}$, depending on specific conditions, such as chloride concentrations and pH values. The scenario becomes even more complex in the presence of CQ, where acid-base properties, tautomerism, and ligands' conformational flexibility may strongly influence the coordination stereochemistry of the metal ion. An accurate description of the system can then be attained by leveraging data from different experimental techniques, each giving valuable and meaningful insights into the complex behavior of an apparently simple system (e.g. ESI-MS in the gas phase, X-ray absorption on frozen and crystalline state, X-ray diffraction of crystalline state, NMR in solution). These different techniques can be integrated by exploiting the tremendous advances of non-empirical molecular dynamics simulations to closely reproduce and rationalize experimental data. Here we present such a combined *in vitro* / *in silico* approach to elucidate the structural determinants of Zn-CQ complexes.

RESULTS AND DISCUSSION

Experimental Studies on Zn-CQ Complexes

NMR and MS. CQ was obtained from commercial racemic CQDP by chemical extraction.[18] NMR analysis confirmed the removal of the phosphate groups: the 1D ^{31}P NMR spectrum of free CQ in DMSO-d_6 shows the absence of any phosphorus signal and the 2D ^{1}H-^{13}C HSQC spectrum shows that protons H5' and H4' are shifted upfield compared to the spectrum of CQDP (Figure S1A-C). Removal of phosphate groups is important as their presence impacts the coordination of Zn^{2+} ions (Figure S1D). A pD-dependent titration allowed to determine the pK_a values of the quinoline nitrogen (pK_{a1} = 7.3 ± 0.2) and the tertiary aliphatic nitrogen (pK_{a2} = 9.5 ± 0.1) by monitoring the chemical shift changes of the neighboring ^{1}H nuclei in 1D NMR spectra (Figrure S2). Moreover, changing the pD values from 13.4 to 3.8, a remarkable downfield shift of the proton bound to the secondary aliphatic nitrogen was observed, with an inflection point of the interpolating curve at a pD value close to pK_{a1}. This shift is due to the protonation of the quinoline nitrogen, which influences the amino/imino tautomerism of the secondary aliphatic nitrogen.[19] The acquisition of 2D ^{1}H-^{13}C HMBC NMR spectra at different pD values allowed to observe a deshielding of the C4 signal (from 149.7 to 155.5 ppm) at lower pD values, confirming the conversion of the secondary aliphatic nitrogen to the imino form (Figure S3).

In order to obtain information on Zn^{2+} coordination, NMR spectra of free CQ in DMSO-d_6 and of an equimolar CQ/$ZnCl_2$ solution were collected at pD of 9.6 (~pK_{a2}). Based on pK_a values, this condition corresponds to a partial protonated state of tertiary amine and a full deprotonated state of quinoline. The 1D ^{1}H NMR spectrum of CQ with 1 equiv of $ZnCl_2$ displayed a deshielding of H9, H3 and NH signals (Figure 1A), while the 1D ^{13}C NMR spectrum showed a decrease in intensity and an upfield shift of C9 and C10 (Figure 1B), supporting Zn^{2+} coordination to the quinoline nitrogen. Complete ^{13}C resonance assignment of CQ in the absence and presence of $ZnCl_2$ was performed by analyzing the 2D ^{1}H-^{13}C HSQC and HMBC spectra (Figure S4). 1D ^{1}H NMR spectra were also recorded at lower pD values (7.9 and 5.9). While at pD 7.9 a behavior similar to that of CQ at pD 9.6 was observed, i.e. deshielding of H9, H3 and NH signals upon Zn^{2+} addition; at acidic pH no variation of chemical shifts was detected, consistent with having a protonated quinoline nitrogen that is not available to coordinate Zn^{2+} (Figure S5).

The ESI-MS spectrum (recorded in positive ion mode) of CQ with 1 equiv of $ZnCl_2$ in DMSO-d_6 displays a main signal at m/z 494.0294 that can be assigned to $[C_{18}H_{27}Cl_4N_3Zn + H]^+$ singly charged species, corresponding to a Zn^{2+} ion coordinated to a CQ molecule and three chlorido ligands. The formation of this complex is also supported by the calculated isotope mass distribution, which closely matches the experimental set of peaks (Figure S6).

Paramagnetic Co^{2+} has been used as a probe to confirm the preferred Zn^{2+} anchoring site, based on the similar coordination properties of the two metal ions.[20,21] NMR monitoring was conducted by performing a titration of free CQ with up to 1 equiv of $CoCl_2$ in DMSO-d_6. The Co^{2+} ion (d^7, high spin) caused paramagnetic shifts and broadening of signals around the coordination site; substoichiometric additions of $CoCl_2$ mostly affected H2, H3 and H9 protons adjacent to the quinoline nitrogen, which experienced the largest line broadening in 1D ^{1}H NMR spectra (Figure S7A). Consistently, the signals of C2, C3, C9 and quaternary carbons C5 and C10 broadened in 1D ^{13}C spectra (Figure S7B). In contrast, the ^{1}H and ^{13}C signals of the aliphatic chain were not affected until the end of the titration, confirming that metal coordination only occurs at the CQ aromatic nitrogen.

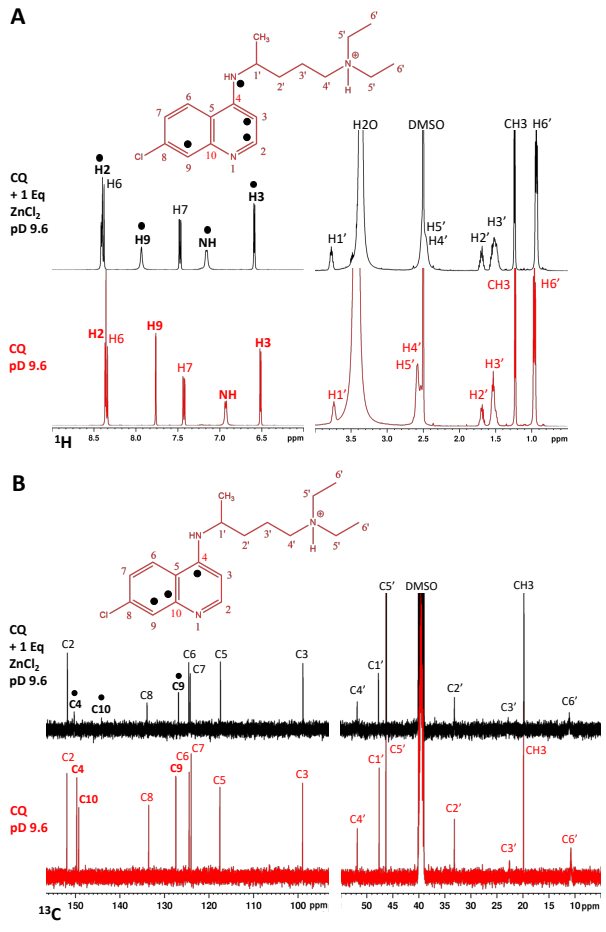

Figure 1. (A) 1D ^{1}H and (B) 1D ^{13}C NMR spectra of free CQ (red) and CQ with 1 equivalent of $ZnCl_2$ (black) in DMSO-d_6 (pD 9.6). The structure of CQ with atom numbering is shown at the top of each panel. ^{1}H and ^{13}C signals experiencing significant shifts upon Zn^{2+} binding are marked with black dots. The assignment is reported on top of each peak. The signals of residual H_2O and DMSO-d_5 are also indicated.

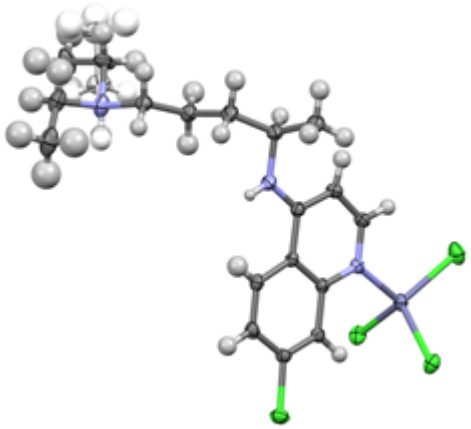

Figure 2. Asymmetric unit of the $Zn(CQH)Cl_3$ complex, with anisotropic ellipsoid representation of non-H atoms. Ellipsoids are shown at the 50% probability level. The atom species are in CPK colors with alternative positions of the disordered ethyl groups in paler colors.

X-ray Crystallography. Small single crystals of the Zn-CQ complex were analyzed by X-ray diffraction at 100 K using synchrotron radiation. The asymmetric unit of the orthorhombic crystals contains one zwitterionic tri-chloro-chloroquinium-zinc complex, $Zn(CQH)Cl_3$ (Figure 2). One ethyl group shows a two-position disorder with 0.5 occupancy factors. The Pbca centrosymmetric space group implies that these crystals are composed by a racemic mixture of the enantiomeric complexes.

The Zn^{2+} ions are coordinated with a distorted tetrahedral geometry (Table S2) by three chlorine ions and by the quinoline N-atom of a chloroquinium (CQH^{+}) ligand (Figure 2). The Zn–N distance of 2.051(1) Å is significantly shorter than that found in the tri-chloro-quinoline-zinc complex by about 0.04 Å.[22] The Zn–Cl bond lengths range from 2.2308(8) to 2.3086(6) Å, with the shortest distance in agreement with the mean value of Zn-Cl bond lengths in tri-chloro-Zn^{2+} complexes coordinated to N(sp^2) ligands (2.239(3) Å).[23] The chloride ion coordinated with the longer Zn–Cl bond length forms an intermolecular H-bond. In fact, the crystal packing of the $Zn(CQH)Cl_3$ complex (Figure S9) shows the assembly of centrosymmetric dimeric species (Figure 3). The dimer is stabilized by two equivalent intermolecular H-bonds involving this coordinated chlorine ion and the protonated tertiary ammine (Cl···N distance of 3.152(2) Å) and by stacking interactions between the aromatic quinoline moieties (interplanar distance of 3.38 Å) as evidenced by the Hirshfeld surface mapped with normalized contact distance (Figure S10). We conclude that the rather distorted tetrahedral geometry of the complex may arise from its dimerization and from relevant intermolecular contacts present in the solid state.

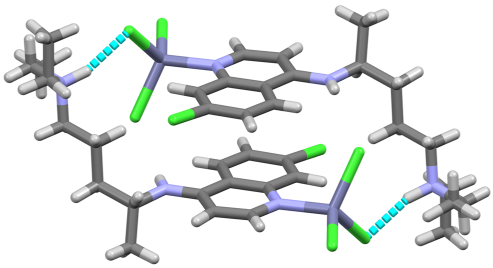

Figure 3. Stick representation of dimeric assembly of the $Zn(CQH)Cl_3$ complex. The atomic species are in CPK colors. For the sake of clarity, only one position of the disordered ethyl group is shown. H-bonds are evidenced with cyan dashed lines. The dimers are located on crystallographic inversion centers.

X-ray Absorption Spectroscopy of Zn-CQ Complexes. X-ray absorption spectroscopy (XAS) was used to probe the coordination properties of zinc bound to CQ. The Zn-CQ complexes in a frozen solution in DMSO (with 10% residual H_2O) and in crystallized form were studied by Zn K-edge XAS to elucidate and compare the coordination sphere around the metal ion in both solution and solid state. The maximum intensity and overall similarity of the normalized X-ray absorption near edge structure spectra (XANES; Figure 4A) indicate a nearly tetrahedral geometry in both complexes.

Extended X-ray absorption fine structure (EXAFS) analysis (Figure 4B, Table S3) of both complexes converge to a four-coordinated zinc. In the case of crystallized Zn-CQ, in agreement with XRD analysis, zinc coordination features three chlorido ligands and one nitrogen atom. Coordination to the quinoline N-atom of CQ is supported by the secondary sphere with three carbon atoms corresponding to the quinoline atoms C2, C9 and C10 (see scheme in Figure 1). For Zn-CQ frozen in DMSO, a decrease of the extended X-ray absorption fine structure (EXAFS) envelope at $k > 6$ Å^{-1} is observed, as compared to the crystallized Zn-CQ, clearly indicating fewer heavy atoms bound to zinc. Indeed, EXAFS analysis reveals that the Zn-CQ complex in solution displays a metal coordination sphere with one nitrogen atom, only two chloride ions and an oxygen-based ligand. A similar coordination sphere was observed for the powder Zn-CQ complex synthesized from DMSO, except for the presence of two more chloride ions at a distance above 3.3 Å, probably due to packing effects (Figure S11, Table S3). Overall these results indicate that the zinc coordination sphere in the Zn-CQ complex in solution is quite similar to that of crystallized Zn-CQ, except that the oxygen ligand in the former is replaced by a chloride ion in the crystal, supporting the notion that three chlorido ligands are favored by crystallization conditions.

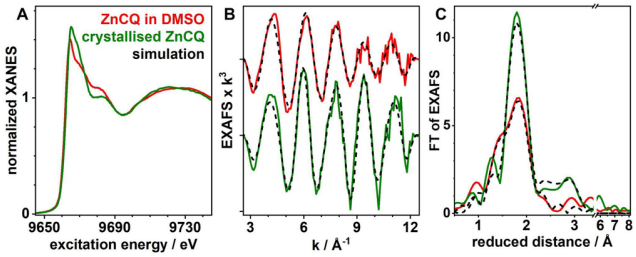

Figure 4. Zn K-edge X-ray absorption spectroscopy (XAS) of Zn-CQ frozen in DMSO-d_6 (red) and in crystallized form (green) reveals a four-coordinated Zn with two chlorido ligands in DMSO and three chlorides in the crystal form. Shown are normalized X-ray absorption near edge structure (XANES; A), extended X-ray absorption fine structure (EXAFS; B) and Fourier transform of EXAFS (C). Black dashed lines in B and C correspond to fits of EXAFS spectra using simulation parameters given in Table S3.

Molecular Dynamics of Zn-CQ Complexes in Aqueous Solution

Our experimental investigations reveal important characteristics of zinc chloride reacting with chloroquine in different protonation states (CQ, CQH^+ and CQH_2^{2+}), in anhydrous conditions and in the presence of DMSO and/or water**.** Specifically, NMR measurements identify the binding site of a Zn^{2+} ion to the quinolinic nitrogen atom of CQ in DMSO/water solution at room temperature. X-ray crystallography studies showed that, under anhydrous conditions in the solid state, (i) the zinc binds to the quinolinic nitrogen atom also here; (ii) three chlorido ligands and CQ form a distorted tetrahedral complex. EXAFS measurements support the notion of a tetrahedral geometry for the Zn-CQ complex, both in frozen DMSO solution and solid state. EXAFS analysis also shows that the Zn^{2+} coordination sphere changes from having three chlorides in the crystal form to two chlorides in the frozen DMSO solution. Finally, ESI-MS spectra reveal the formation of a tetra-coordinate complex $[Zn(CQH_2)Cl_3]^+$ in the gas phase. Taken together, these experiments suggest that the Zn^{2+} ion in water solution binds to one CQ molecule in its quinolinic nitrogen, with chlorido ligands and water molecules completing a tetrahedral coordination. A penta-coordinated chloro complex, such as that as originally proposed by Navarro *et al.*[15] ($[ZnCl_2(CQ)(H_2O)_2]$) might also exist in aqueous solution.

Here, the structural dynamics of the latter, along the tetra- and penta-coordinated complexes in Figures 5 (left) and 6 are investigated by *ab initio* molecular dynamics (AIMD) simulations at room temperature, using the BLYP and B3LYP exchange-correlation functionals.[24] The complexes are immersed by around 110 water molecules, and the entire system is treated from first principles. Thus, in our simulation setup, the ligands may enter or abandon the Zn^{2+} coordination sphere during the dynamics.

Approx 15 ps of simulations for each complex was used for analysis and for comparison with the NMR and EXAFS data measured in this work. Additionally, approx 5 ps simulations were collected for specific complexes at the more accurate (and far more expensive) B3LYP level of theory. We use a truncated model of the chloroquine molecule (indicated as CQ_m) in which the aliphatic chain is replaced by a methyl group for computational convenience. This replacement is expected not to affect Zn^{2+} coordination chemistry. This is supported by NMR measurements with Co^{2+} that do not show the formation of chelates (Figure S7). O

Our AIMD simulations suggests that the proposed chloro-aquo complex $[Zn(CQ_m)Cl_2(H_2O)_2]$ from the work of Navarro *et al.*[15] is not stable in water (Figure 5). It loses a water ligand readily in the sub-ps timescale to yield $[Zn(CQ_m)Cl_2(H_2O)]$ (**CL2**). This finding is corroborated by quantum chemical calculations, which favors unambiguously the tetra-coordination over a penta-coordination in implicit solvent at the DLPNO-CCSD(T1)/def2-(S/TZ)VP//B3LYP/def2-TZVP[25–30] level of theory (Section 5 in SI).[31] We next discuss the simulations of the complexes in Figure 6**;** all of them featuring the Zn-CQ moiety with water and/or chlorido ligands.

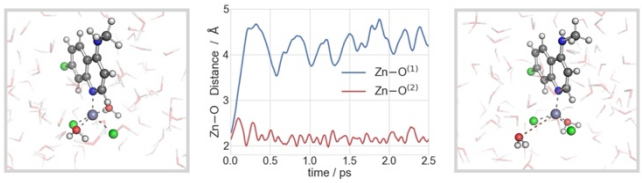

Figure 5. A water molecule dissociates from the $[Zn(CQ_m)Cl_2(H_2O)_2]$ complex (left) to form $[Zn(CQ_m)Cl_2(H_2O)]$ (**CL2,** right) in the AIMD. The plot in the middle reports the distances between the two water ligands and the zinc ion as a function of simulation time. One of them dissociates from the zinc ion already after 0.5 ps of AIMD.

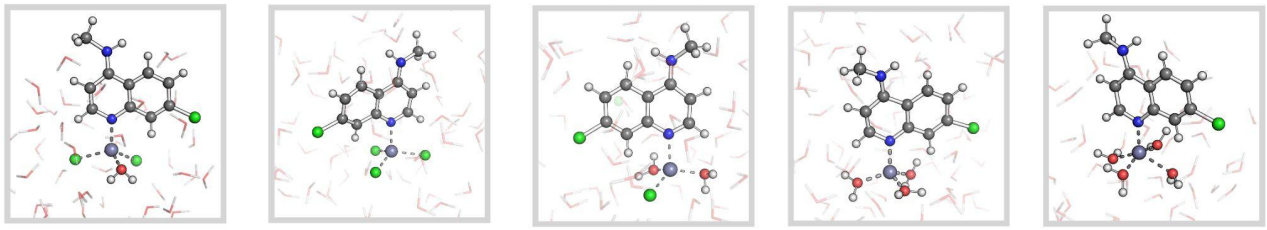

CL2 – $[Zn(CQ_m)Cl_2(H_2O)]$ **CL3** – $[Zn(CQ_m)Cl_3]^-$ **CL** – $[Zn(CQ_m)Cl(H_2O)_2]^+$ **WAT3** – $[Zn(CQ_m)(H_2O)_3]^{2+}$ **WAT4** – $[Zn(CQ_m)(H_2O)_4]^{2+}$

Figure 6. Overview of Zn-CQ_m complexes with varying numbers of chloride and water ligands from AIMD simulations in aqueous solution.

CL2 features two coordinating chloride ions and one water molecule to complete a distorted tetrahedral coordination of the metal ion. The electrostatic repulsion of the chloride ions causes a significantly larger $Cl^{(1)}$–Zn–$Cl^{(2)}$ angle of 114° ± 6°, as compared to the O–Zn–$Cl^{(1)}$ and O–Zn–$Cl^{(2)}$ angles of 103° ± 6° and 105° ± 7°, respectively. The calculated coordination bond distances of the Zn–N^{CQ}, Zn–$O^{(1)}$, Zn–$Cl^{(1)}$ and Zn–$Cl^{(2)}$ bonds are 2.07 ± 0.07, 2.10 ± 0.08, 2.35 ± 0.09 and 2.29 ± 0.06 Å, respectively (see SI for details). The chloride ions form hydrogen bonds to the water. These interactions weaken the metal-ligand bond and thus are expected to cause an increase of the bond lengths. Indeed, because of this and of the relative large atomic size of chloride, the Cl–Zn bonds are, ~0.2 Å longer than the water- and CQ_m-Zn bonds. Zn-atom donor bond lengths are likely to be overestimated by BLYP-based calculations.[32,33] Indeed, they turn out to be shortened by up to 0.05 Å when using the more accurate B3LYP functional (Table S4).

Next, we turn our attention to electronic properties: (i) The Mulliken charge of the Zn^{2+} ion is +0.85 ± 0.03 *e*, suggesting that charge transfer from the ligands increases the electronic charge density at the Zn^{2+} ion. This effect has been already observed for Zn-complexes and Zn^{2+} ions bound to proteins by pioneering studies of Merz and coworkers.[34–36] In fact, fluctuating Zn^{2+} charges comprise a major challenge for the simulation of Zn^{2+} complexes[34–36], which is fully addressed here by AIMD. (ii) The Wannier Centers (WCs) along chemical bonds can be used to describe their polarity.[37] The WCs along the Zn–N^{CQ}, Zn–$Cl^{(1/2)}$ and Zn–$O^{(1)}$ bonds are located at the donor atoms with fractional distance (defined as the difference between the Zn–WC and ligand atom–WC distances, which are normalized to the correspondent bond length) of ~0.75, ~0.75 and ~0.83 from the metal ion, respectively. These results indicate a slightly stronger polarization of the CQ_m and chlorido ligands compared to the water molecule, consistent with the well-known Hard-Soft Acid-Base concept.[38]

CL3 results from replacement of a Zn-bound water in **CL2** with chloride. The simulation reveals a stable, almost regular, tetra-coordinated complex with averaged Zn–Cl distances in the range of 2.35–2.37 Å and Cl–Zn–Cl angles between 107° and 109°, reflecting the equivalence of the chlorido ligands in solution. The hydrogen bonds weaken the coordination bonds as discussed and thus are expected to cause an increase of the bond lengths, which indeed is the case (see also Figure S9 and Table S2 in SI). The average Zn–N^{CQ} bond distance of 2.07 ± 0.06 Å is similar to that observed for **CL2** (Table S4).[39]

The Mulliken charge of the Zn^{2+} ion (+0.78 ± 0.03 *e*) is lower than that of **CL2,** possibly because the chlorido ligands are more polarizable than water. The fractional distances of WCs are comparable to those of Zn–N^{CQ} and Zn–Cl bonds (~0.75).

We finally analyze two tetrahedral complexes (featuring a number of chloride and water molecules not emerging from experiments: (i) In **CL** (Figure 6), a chloride in **CL2** is replaced by a water molecule**. CL** retains a distorted tetrahedral coordination, with the $Cl^{(1)}$–Zn–$O^{(1/2)}$ angles (both 110° ± 7°) larger than the $O^{(1)}$–Zn–$O^{(2)}$ angle (102° ± 7°). The Zn–N^{CQ} and Zn-$Cl^{(1)}$ bond lengths are shortened by ~0.05 Å relative to **CL2** and **CL3** (see SI for details), possibly because the effective charge of the zinc ion (+0.94 ± 0.03 *e*) increases on passing from **CL** to **CL2/3.** In turn, this might be caused by the fact that the water ligand is less polarizable than chloride. The Zn–O bond lengths are also slightly shortened relatively to the one in **CL2** for increased charged on the metal ion (Table S4). (ii) In **WAT3**, no chloride ligand is present. The Zn^{2+} effective charge further increases (+1.03 ± 0.04 *e*), while the Zn–N^{CQ} and Zn–O bond lengths decrease by ~0.2–0.3 Å relative to **CL** (Table S4). Remarkably, in a simulation replica with different initial positions and velocities than the first one, a fourth water molecule binds to the metal ion to form the penta-coordinated complex **WAT4**. Its geometry is in between a square pyramidal and trigonal bipyramidal structure. The average Zn–N^{CQ} distance is found to be 2.06 ± 0.06 Å, slightly larger than that in **WAT3** (2.02 ± 0.06 Å). The Zn–O distances of **WAT4** are longer than those of **WAT3** and also show larger fluctuations. AIMD simulations on **WAT4** using the more accurate (and expensive) B3LYP functional show that the coordination bond lengths are, as expected, shortened, while the Zn–O bond lengths still fluctuate, but less so (Table S4). We conclude that both Zn-CQ-aquo complexes (**WAT3** and **WAT4**) may be present as intermediate species in aqueous solution and demonstrate the flexibility of zinc coordination chemistry, as previously observed: Indeed, theoretical studies predicted the presence of two different coordinations on Zn^{2+}-diamine-aquo complexes[40] and transient conversion of tetra- and penta-coordination may play a role for zinc-dependent alcohol dehydrogenase function.[41,42]

Comparison with NMR data. In the pool of experimental data reported here, the NMR experiments in solution reflect the most similar conditions to the water solution environment simulated by the theoretical calculations. The difference in the solvent conditions between experiment (90% DMSO /10% water) and theory (water) is expected to have a minor effect on the chemical shifts, because both solvents are highly polar and no hydrogen bond acceptors, beside the chlorine atom bonded to the C8 atom of CQ, are present in the complexed CQ ligand. Figure 7 (and Figures S13-S14) show the distributions of the ^{1}H and ^{13}C chemical shifts calculated using M06L[43] and B3LYP[28,29] functionals. The latter have been shown to predict accurately chemical shifts.[44]

Our predictions are consistent with experiments. The distributions of the calculated signals are much broader than the experimental ones.[45]

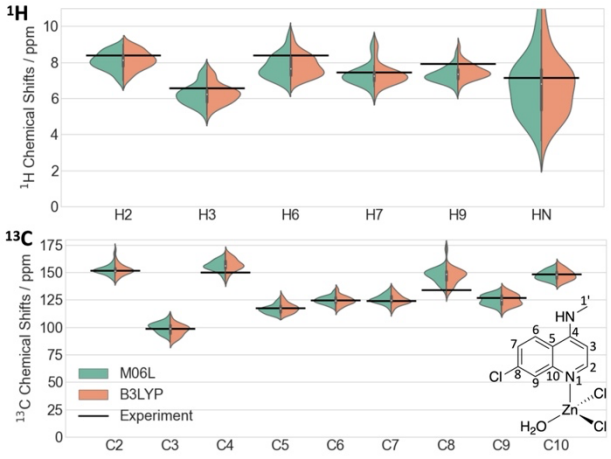

Figure 7. Calculated ^{1}H and ^{13}C NMR chemical shift distributions using DFT with M06L[43] and B3LYP[28,29] functionals for complex **CL2,** compared with experimental data (black lines). Insets: Structural formula of complex **CL2** indicating the atom numbering.

^{1}H spectra. H2 and H6 nuclei (Figure 7) are the most deshielded nuclei, experimentally observed at 8.41 and 8.39 ppm, respectively. The calculated chemical shifts cover this spectral region, with fluctuations between 7.5 – 8.5 ppm. In contrast, the H3 nucleus is predicted to resonate around 6 ppm, consistent with the experimentally measured value of 6.59 ppm. Also, the predictions of H7 and H9 are consistent with the experimental spectrum. The calculated HN chemical shifts show a very broad distribution. This is not surprising since it involves hydrogen bonds to solvent molecules which sensitively modulate the electronic density at the HN nucleus.

^{13}C spectra. The nuclei C2, C4 and C10 are predicted to resonate around 150 ppm, in excellent agreement with experiment (151.8, 150.2 and 148.4 ppm, respectively). These nuclei are directly bonded to nitrogen atoms, either to the quinolinic nitrogen or the exocyclic amine group, which cause the downfield shift. The calculations also reproduce the experimentally observed aromatic signal at 98.9 ppm for the C3 nucleus. In between, we identified, consistently with experiment, the C5, C6, C7 and C9 nuclei of the CQ ligand. The largest discrepancy is observed for the chemical shift distribution of the C8 nucleus. The calculated shifts fluctuate around ~150 ppm, while the experimental signal peaks at lower fields of 133.7 ppm. This carbon atom is bonded to a chlorine, which can act as a hydrogen bond acceptor in water solution. In turn, water can polarize the chlorine atom, which makes it a stronger electron withdrawing substituent. As a result, the C8 signal is shifted downfield in comparison to the experimental signal in DMSO.

Comparison with EXAFS data. The conditions in our simulations (water at 300 K) differ significantly from the experimental one (frozen solution of DMSO with 10% residual H_2O at 20 K). The k^3-weighted spectrum and Fourier transform of **CL2** best reproduces the experimental spectrum for the Zn-CQ complex (Figures 8 and S15). The calculations are carried out at the B3LYP level of theory. In spite of the different conditions, the averaged Zn–N^{CQ} bond distances agree well with experiment (Tables S3 and S4). The Zn–O and Zn–Cl distances in the calculated structures are larger than those derived from the EXAFS fit by ~0.08–0.1 Å, possibly due to hydrogen bonding interactions with the solvent that weakens the metal-ligand bonds, as discussed previously. On the other hand, the Fourier transform of the spectrum differs slightly. In particular, a shoulder at low effective distances (~1.5 Å), that arises from the N^{CQ} and O donor atoms (see discussion above), is resolved only in the experimental spectrum. The difference can be explained by temperature effects, which cause larger fluctuations in the bond distances at room temperature conditions.

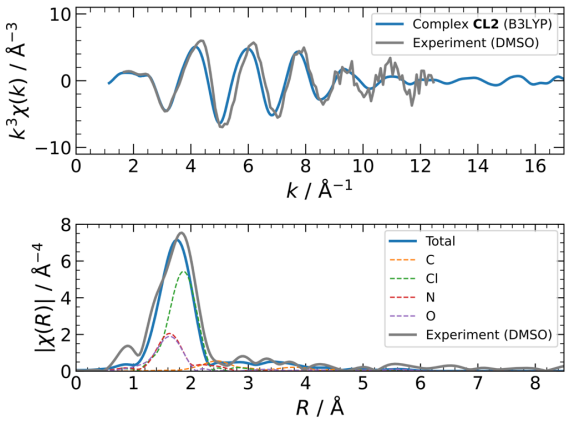

Figure 8. k^3-weighted EXAFS spectrum (top) and Fourier Transform (bottom) calculated from the AIMD-B3LYP simulation of **CL2** in comparison to the experimental spectrum.

Comparison with X-ray data. The calculated Zn–N^{CQ} bond lengths and one of the Zn-Cl bond of **CL3** compare fairly well with those in the X-ray structure (Tables S2 and S4). The other two Zn–Cl bonds are far shorter in the X-ray structure, because unlike the first, they are not involved in H-bonding interactions (Figure 3). The calculated, tetrahedral geometry of the complex differs markedly from that in the X-ray structure, which is distorted because of packing forces present only in the crystal.

In conclusion, our simulations reproduce fairly well the observed experimental spectral properties of Zn-CQ complexes, within the limitations associated with the limited time scale investigated. The calculations allow us to suggest a tetra-coordination in solution when chloride is bound (complexes **CL, CL2, and CL3**) or a mixture of a tetra- and penta-coordination when only water is present (complexes **WAT3** and **WAT4**).

CONCLUSIONS

The interaction of the zinc ion with low molecular weigth ligands, such as water, inorganic anions and organic molecules, is highly relevant in biology, but, contrary to its coordination in proteins, it has been poorly discussed in the biochemical literature.[46] Most of the studies rely on crystal structures, which allow only a few snapshots of the system but may not reproduce the complex behavior/dynamics in solution revealed by modern molecular spectroscopy methods.

Here we studied the effect of adding $ZnCl_2$ to purified CQ. The Zn^{2+} complex was characterized by a combination of state-of-the-art molecular simulations along with solution NMR, ESI-MS, X-ray absorption and diffraction methods. The CQ coordination turns out to be strictly related to its acid-base properties and to the protonation state of nitrogen atoms, which in turn are linked to the ability of CQ to cross biological membranes and accumulate into acidic organelles. In the physiological pH range, CQ binds to Zn^{2+} through the quinoline ring nitrogen in a tetrahedral complex with three chloride ions or two chloride ions and a water molecule completing the coordination sphere to yield a zwitterionic or cationic complex, respectively (Chart 1). The former is stable at neutral pH and at high chloride concentrations typical of the extracellular medium; however, metal coordination is lost at moderately low pH, suggesting the release of Zn^{2+} ions into the lysosomal lumen. The two complexes can be derived from the reaction of CQ with the two most abundant species present in a $ZnCl_2$ solution, namely $[ZnCl_3(H_2O)]^-$ and $[ZnCl_2(H_2O)_2]$,[47] by substitution of a water molecule. AIMD simulations of these complexes are fully consistent with the experimental data and further suggest the existence of aqueous species with higher water content (Chart 1). Among the complexes in Chart 1, $[Zn(CQH)Cl_2(H_2O)]^+$ is not only fully consistent with NMR, but it also is the complex that best reproduces the EXAFS spectral data.

Overall, our combined *in vitro / in silico* approach has elucidated the structural determinants of Zn-CQ complexes, and it can be applied to other metal-targeting drugs and bio-inorganic systems.

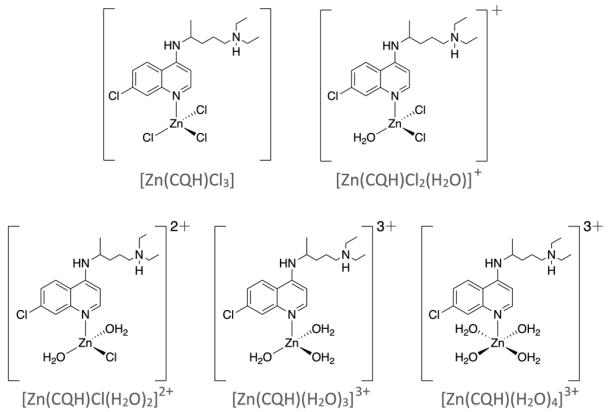

Chart 1.

EXPERIMENTAL AND COMPUTATIONAL SECTION

NMR. CQ has been obtained from commercial CQDP by chemical extraction, following a procedure reported in the literature.[18] Elemental analysis and Nuclear Magnetic Resonance (NMR) were performed to check the purity of the extracted ligand. Calculated values for $C_{18}H_{26}N_3Cl \cdot 2\ H_3PO_4 \cdot 2\ H_2O \cdot 2\ CH_3OH$ (CQDP) were: C 38.99%; H 7.19%; N 6.82%. Found values were: C 39.43 %; H 8.25%; N 7.39 %. For purified CQ, calculated for $C_{18}H_{26}N_3Cl$: C 67.58 % H 8.19 %; N 13.13 %. Found: C 67.34 %; H 7-05 %; N 13.03 %. The Zn-CQ complex was prepared in solution by adding 1 equiv of $ZnCl_2$ in 500 µL of CQ DMSO-d_6 solution (4.5 mM or 9 mM).

NMR samples were prepared by dissolving CQ with and without 1eq of $ZnCl_2$ in DMSO-d_6 at 4.5 mM or 9 mM concentration, and the pD was adjusted with $DClO_4$ or NaOD using the relationship pD = pH* + 0.4 (where pH* is a direct reading in D_2O solution of the H_2O-calibrated pH-meter). 1D ^1H and 2D ^1H-^{13}C HSQC and HMBC NMR spectra were recorded at 298.15 K on a Bruker Avance 300 Ultrashield spectrometer equipped with a double resonance broad-band probe with Z-Gradient. 1D ^1H NMR spectra were acquired with a relaxation delay of 1.5 s, 64 scans, 32K data points and a spectral width of 21 ppm. 2D ^1H-^{13}C HSQC and HMBC spectra were acquired with a recycle delay of 1.5 s. Each time domain was the average of 64 scans consisting of 1K complex data points over an F2 (^1H) spectral width of 13.35 ppm; the second dimension was derived from 256 increments with an F1 (^{13}C) spectral width of 250 ppm centered at 75 ppm. For HSQC spectra, an INEPT delay $1/(4 \cdot {}^1J_{C\text{-}H})$ of 1.72 ms ($^1J_{C\text{-}H}$ = 145 Hz) was used and decoupling during acquisition was achieved using the standard GARP scheme. 1D ^{13}C NMR spectra were acquired on an Agilent 500/54 Premium Shielded spectrometer and with power-gated decoupling using a 20° flip angle and a relaxation delay of 2.0 s. Each spectrum consisted of 16K scans, 32K data points and a spectral width of 300 ppm (^{13}C carrier at 130 ppm). All data were processed with Bruker software Topspin™ (version 3.5). Before Fourier transformation, an exponential multiplication with a line broadening (LB) of 0.30 Hz and 2 Hz was applied for 1D ^1H and 1D ^{13}C spectra, respectively. 2D spectral data, zero-filled in F1 to 1K data points, were subjected to apodization using a squared cosine bell function in both dimensions prior to Fourier transformation and phase correction. ^1H and ^{13}C chemical shifts were referenced to residual DMSO-d_5 (δ^1H = 2.50 ppm and $\delta^{13}C$ = 39.52 ppm).

NMR-monitored pD titration experiments were used to determine site-specific pK_a values of CQ. The ligand was dissolved in 500 µL of DMSO-d_6 and transferred to an NMR tube. The pD of the sample was adjusted to the required value by adding $DClO_4$ or NaOD solutions and measured using a 3 mm diameter electrode for NMR tubes. The pD-titration curves were fitted using the following equation through GraphPad Prism 7.0 software:

$$\delta_{obs} = \delta_p + \frac{\Delta\delta}{1 + 10^{(pKa - pD)}} \qquad (1)$$

where δ_{obs} is the chemical shift observed at each pD value, δ_p is the chemical shift of the fully protonated species and $\Delta\delta$ is the chemical shift variation between the end and the beginning of the titration.[48]

X-ray Crystallography. Single crystals suitable for X-ray investigation were obtained by slow cooling and evaporation of a methanol solution of racemic chloroquine and zinc chloride in a 1:1.4 molar ratio (detailed description of the synthesis in SI). Large rectangular transparent crystals were obtained after one day (Figure S8).

Data collection was carried out at the XRD1 beamline of the Elettra synchrotron (Trieste, Italy), employing the rotating-crystal method with a Dectris Pilatus 2M area detector. The crystal was cryoprotected with Parabar 10312 and kept under a nitrogen stream at a 100 K during data collection. The structure was solved using direct methods and refined by full-matrix least-squares (FMLS) methods on F^2, with anisotropic thermal parameters for all non-hydrogen atoms. Crystallographic data and refinement details are reported in Table S1 and in SI.

X-ray absorption spectroscopy (XAS). XAS at the Zn K-edge was performed at beamline KMC-3 at BESSY-II (Berlin, Germany) using the previously described set-up: Storage ring operated in top-up mode at 300 mA, double crystal Si[111] monochromator with ~2 eV bandwidth, 13-element energy-resolving silicon-drift detector (RaySpec) for fluorescence monitoring, sample held in a cryostat (Oxford) at 20 K.[49] The X-ray spot size on the sample was set by a focusing mirror and slits to about 4.0 mm × 1.5 mm. XAS at the Zn K-edge was also performed at the synchrotron SLS (Villigen, Switzerland) at the SuperXAS superbending-magnet beamline with the storage ring operated in top-up mode (400 mA) using a setup for XAS as previously described.[50] Signal-to-noise ratios were improved by averaging up to 4 spectra collected on different sample spots to avoid any unlikely photodamage for Zn^{2+} complexes. XAS spectra were averaged after detector dead-time and self-absorption correction, normalized to derive X-ray absorption near edge structure (XANES) spectra, and extended X-ray absorption fine structure (EXAFS) spectra were extracted as described earlier.[51] The monochromator energy axis was calibrated (accuracy ± 0.1 eV) using the first inflection point at 9659 eV in the simultaneously measured absorption spectrum of a Zn foil as a standard. Averaging, normalization, and extraction of EXAFS oscillations and conversion of the energy scale to the wave-vector (k) scale were performed as previously described.[49] The k^3-weighted EXAFS spectra were simulated ($S0^2$ = 1.00) by a least-squares procedure using phase functions calculated with FEFF8-lite[52] and Fourier transforms (FTs) were calculated using the in-house software SimX using k-range of 1.7–12.4 $Å^{-1}$, cos windows extending over 10% at both k-range ends.[53,54] SimX uses the Levenberg–Marquardt (damped least-squares) algorithm. The E0 used for extraction of EXAFS oscillations was 9659 eV, and E0 was refined to about (9654 ± 1) eV in the EXAFS fitting.

AIMD in explicit water. The first system simulated here is the $[Zn(CQ)Cl_2(H_2O)_2]$ complex, with the chloride and water ligands in *trans* position. The aliphatic side chain at CQ exocyclic nitrogen was replaced by a methyl group to reduce the system size without significantly affecting the interactions of the zinc ion binding to the quinolinic nitrogen (model "CQ_m"). The complex was pre-optimized at B3LYP/def2-SVP in gas phase[28–30] and then solvated in a pre-equilibrated water box of 15.0×16.8×15.7 Å using the GROMACS `solvate` tool.[55] The resulting system consisted of 112 water molecules and 361 atoms in total. This corresponds to a bulk water density of 0.89 $g \cdot mL^{-1}$, commonly observed in AIMD simulations.[56,57] The quantum problem was solved using planewave-based DFT.[58] We employed the BLYP functional with a planewave cutoff of 100 Ry and norm-conserving Troullier-Martins pseudopotentials.[59] The system was initially optimized for 1,100 steps. AIMD simulations within the Born-Oppenheimer scheme were carried out in the NVT ensemble. A time step of 0.48 fs was used. The system was first heated up with a rate of 0.024 $K \cdot fs^{-1}$ to 300 K in 0.96 ps using the Berendsen thermostat with a coupling constant of 5,000 a.u.,[60] followed by additional 0.96 ps for relaxation of the solvent at 300 K. In this preparation process, the coordinates of the complex were constrained. Then, the system was free to evolve for 19.2 ps at 300 K. The temperature was kept constant using a Nosé-Hoover thermostat, with a frequency of 5,000 cm^{-1}.[61,62] The system quickly lost a water molecule to form **CL2** (Figure 5). The last 14.4 ps were used for analyses of **CL2**. The other tetra complexes in Figure 6 were built from **CL2** by replacing a chloride with a water molecule or the other way around. They then followed the same computational protocol, undergoing 19.2 ps AIMD simulations at 300 K. **CL2** and **WAT4** (Figure 6) underwent 5.28 ps AIMD with the B3LYP exchange-correlation functional, starting from the final AIMD snapshots using BLYP. The same setting as above was used, except that here we used a multiple time step framework for which high level forces were evaluated at B3LYP, and intermediate steps at BLYP.[63] Benchmark calculations revealed a time step factor of 5 as a reasonable choice (Figure S12). The last 4.80 ps were collected for analysis. AIMD-BLYP simulations of CQ_m in water were also run. The initial structure was obtained by replacing the zinc and chloride ions with water molecules in **CL2.** It underwent 19.2 ps of AIMD-BLYP at 300 K using the same computational protocol as above. 14.8 ps were collected for analysis. The calculations were carried out with CPMD 4.3.[64] The following properties were calculated: (i) geometrical quantities (and WCs[37]), calculated every 4.8 fs (0.24 ps) of AIMD-BLYP. (ii) ^1H and ^{13}C NMR chemical shifts (CSs) and the Mulliken charges were calculated every 0.48 ps of AIMD-BLYP, using ORCA 5.0.1.[44,65] The CSs were calculated as mean traces of chemical shielding tensors of systems containing the Zn^{2+} ion, the CQ_m ligand, the chloride ions and water molecules with a 5 Å distance around the Zn-CQ_m moiety (149 to 185 atoms). The tensors were obtained using the coupled perturbed self-consistent field approach, using the gauge-including atomic orbitals, as implemented, and benchmarked for the ORCA program.[44,65] The M06L[43] and B3LYP[28,29] functionals, along with the pc-sSeg-2 basis set, were used.[66] Two-electron Coulomb integrals were approximated with the resolution-of-the-identity method using the auxiliary def2-TZVP/JK basis set,[67,68] while the chain-of-sphere algorithm was employed for the two-electron exchange terms.[69] ORCA's very tight convergence settings and large grid specification were used.[65] Polarization from the bulk water phase was included by the conductor-like polarizable continuum model using a dielectric constant of 80.4.[70] The calculated CSs were then shifted to an appropriate reference value by averaging the calculated CSs of H7/C7 nuclei in CQ_m and setting to zero the difference between those and the correspondent experimental values. We subtracted then all the calculated CSs by the quantities required to set these differences to zero. (iii) EXAFS spectra at the zinc edge, calculated every 0.048 ps from the AIMD-BLYP and AIMD-B3LYP using FEFF6L[71–73] . The zinc ion, the water molecules within 7.5 Å from it, the CQ_m ligand as well as the chloride ions were included in the calculations (136 to 207 atoms). A real phase space shift of 5 eV was used. The real-space representation was then determined by Fourier transformation of the k^3-weighted EXAFS spectra using the Larch module implemented in Python.[74] For this purpose, the spectral data in the *k*-vector interval of 2.5 to 12.5 $Å^{-1}$ and the Kaiser-Bessel window function was applied. Atom type specific contributions were identified through their backscattering contributions. All properties were obtained as averages, except for the CSs, that are presented here as distributions in Figure 7.

ASSOCIATED CONTENT

Supporting Information

Experimental details for ESI-MS and crystallography; detailed NMR spectral analyses; ESI-MS spectrum and calculated isotope mass distributions; crystallographic refinement data and X-ray analyses; EXAFS spectra in powder and analyses; AIMD structural data, calculated NMR chemical shifts and simulated EXAFS spectra; quantum chemical calculations (PDF).

AUTHOR INFORMATION

Corresponding Authors

*Paolo Carloni – *Computational Biomedicine (IAS-5/INM-9), Forschungszentrum Jülich GmbH, 52428Jülich, Germany; Department of Physics, RWTH Aachen University, 52062 Aachen, Germany;* Email: p.carloni@fz-juelich.de
Liliana Quinatar – *Department of Chemistry, Cinvestav, 07480 Mexico City, Mexico;* Email: lilianaq@cinvestav.mx
Fabio Arnesano – *Department of Chemistry, University of Bari "Aldo Moro", 70125 Bari, Italy;*
Email: fabio.arnesano@uniba.it

Author Contributions

‡M.P., D.V., F.K.S. and N.S. contributed equally to this work.

ACKNOWLEDGMENT

The authors thank Prof. Katrin Amunts (Jülich Research Center) for suggesting us to investigate zinc as an antiviral agent and Prof. Michele Parrinello (Italian Institute of Technology) for fruitful scientific discussion. FA, DV, AB thank the University of Bari, the Consorzio Interuniversitario di Ricerca in Chimica dei Metalli nei Sistemi Biologici (CIRCMSB) and the Italian Ministero dell'Università e della Ricerca [PRIN 2017WBZFHL to F.A.] for support. The Paul Scherrer Institut (PSI), Villigen, Switzerland and the Helmholtz-Zentrum Berlin für Materialien und Energie are acknowledged for provision of synchrotron radiation beamtime at beamlines SuperXAS at SLS and KMC-3 at BESSY II, respectively. Authors acknowledge technical support by Urs Vogelsang at the SuperXAS beamline, and the staff at the KMC-3 beamline. Covid19 related funding from the Government of Hidalgo, Mexico, facilitated synchrotron experiments at the Swiss Light Source (SLS) in PSI. Support by the German Bundesministerium für Bildung und Forschung (BMBF) is gratefully acknowledged (Grant 05K19KE1, operando-XAS, to Holger Dau). Nils Schuth is a Deutsche Forschungsgemeinschaft international fellow (SCHU 33411/2-1). GR acknowledges the Federal Ministry of Education and Research (BMBF) and the state of North Rhine-Westphalia as part of the NHR Program. GR and PC acknowledge the Joint Lab "Supercomputing and Modeling for the Human Brain" of the Helmholtz Association. The authors gratefully acknowledge the Gauss Centre for Supercomputing e.V. (www.gauss-centre.eu) and the Jülich Supercomputer Center for providing the computing time for this project.

REFERENCES

(1) Rynes, R. I. Antimalarial Drugs in the Treatment of Rheumatological Diseases. *Rheumatology* **1997**, *36* (7), 799–805. https://doi.org/10.1093/rheumatology/36.7.799.

(2) Wu, R.; Wang, L.; Kuo, H.-C. D.; Shannar, A.; Peter, R.; Chou, P. J.; Li, S.; Hudlikar, R.; Liu, X.; Liu, Z.; Poiani, G. J.; Amorosa, L.; Brunetti, L.; Kong, A.-N. An Update on Current Therapeutic Drugs Treating COVID-19. *Current Pharmacology Reports* **2020**, *6* (3), 56–70. https://doi.org/10.1007/s40495-020-00216-7.

(3) Warhurst, D. C. Hydroxychloroquine Is Much Less Active than Chloroquine against Chloroquine-Resistant Plasmodium Falciparum, in Agreement with Its Physicochemical Properties. *Journal of Antimicrobial Chemotherapy* **2003**, *52* (2), 188–193. https://doi.org/10.1093/jac/dkg319.

(4) Homewood, C. A.; Warhurst D. C.; Peters, W.; Baggaley, V. C. Lysosomes, PH and the Anti-Malarial Action of Chloroquine. *Nature* **1972**, *235* (5332), 50–52. https://doi.org/10.1038/235050a0.

(5) Krogstad, D. J.; Schlesinger, P. H. A Perspective on Antimalarial Action: Effects of Weak Bases on Plasmodium Falciparum. *Biochemical Pharmacology* **1986**, *35* (4), 547–552. https://doi.org/10.1016/0006-2952(86)90345-X.

(6) Schultz, K. R.; Gilman, A. L. The Lysosomotropic Amines, Chloroquine and Hydroxychloroquine: A Potentially Novel Therapy for Graft-Versus-Host Disease. *Leukemia & Lymphoma* **1997**, *24* (3–4), 201–210. https://doi.org/10.3109/10428199709039008.

(7) Al-Bari, Md. A. A. Targeting Endosomal Acidification by Chloroquine Analogs as a Promising Strategy for the Treatment of Emerging Viral Diseases. *Pharmacology Research & Perspectives* **2017**, *5* (1), e00293. https://doi.org/10.1002/prp2.293.

(8) Savarino, A.; Boelaert, J. R.; Cassone, A.; Majori, G.; Cauda, R. Effects of Chloroquine on Viral Infections: An Old Drug against Today's Diseases. *The Lancet Infectious Diseases* **2003**, *3* (11), 722–727. https://doi.org/10.1016/S1473-3099(03)00806-5.

(9) Xue, J.; Moyer, A.; Peng, B.; Wu, J.; Hannafon, B. N.; Ding, W.-Q. Chloroquine Is a Zinc Ionophore. *PLoS ONE* **2014**, *9* (10), e109180. https://doi.org/10.1371/journal.pone.0109180.

(10) te Velthuis, A. J. W.; van den Worm, S. H. E.; Sims, A. C.; Baric, R. S.; Snijder, E. J.; van Hemert, M. J. Zn2+ Inhibits Coronavirus and Arterivirus RNA Polymerase Activity In Vitro and Zinc Ionophores Block the Replication of These Viruses in Cell Culture. *PLoS Pathogens* **2010**, *6* (11), e1001176. https://doi.org/10.1371/journal.ppat.1001176.

(11) Wessels, I.; Fischer, H. J.; Rink, L. Dietary and Physiological Effects of Zinc on the Immune System. *Annual Review of Nutrition* **2021**, *41* (1), 133–175. https://doi.org/10.1146/annurev-nutr-122019-120635.

(12) Derwand, R.; Scholz, M. Does Zinc Supplementation Enhance the Clinical Efficacy of Chloroquine/Hydroxychloroquine to Win Today's Battle against COVID-19? *Medical Hypotheses* **2020**, *142*, 109815. https://doi.org/10.1016/j.mehy.2020.109815.

(13) Carlucci, P. M.; Ahuja, T.; Petrilli, C.; Rajagopalan, H.; Jones, S.; Rahimian, J. Zinc Sulfate in Combination with a Zinc Ionophore May Improve Outcomes in Hospitalized COVID-19 Patients. *Journal of Medical Microbiology* **2020**, *69* (10), 1228–1234. https://doi.org/10.1099/jmm.0.001250.

(14) Indeed, the U.S. Food and Drug Administration (FDA) has revoked the authorization for emergency use of CQ and hydroxychloroquine and the NIH has recommended against their usse for COVID-19 except in clinical trials [https://www.covid19treatmentguidelines.nih.gov/therapies/antiviral-therapy/chloroquine-or-hydroxychloroquine-and-or-azithromycin/] (accessed 2022-06-15).

(15) Navarro, M.; Goitia, H.; Silva, P.; Velásquez, M.; Ojeda, L. E.; Fraile, G. Synthesis and Characterization of New Copper– and Zinc–Chloroquine Complexes and Their Activities on Respiratory Burst of Polymorphonuclear Leukocytes. *Journal of Inorganic Biochemistry* **2005**, *99* (8), 1630–1636. https://doi.org/10.1016/j.jinorgbio.2005.05.002.

(16) Navarro, M.; Hernández, C.; Vásquez, F.; Goitia, H.; Ojeda, L. E.; Velásquez, M.; Fraile, G. Syntheses, Characterization, and Biological Evaluation of New Zinc-and Gold-Chloroquine Diphosphate Complexes. *Transition Metal Chemistry* **2008**, *33* (7), 893–898. https://doi.org/10.1007/s11243-008-9129-0.

(17) Helm, L.; Merbach, A. E. Water Exchange on Metal Ions: Experiments and Simulations. *Coordination Chemistry Reviews* **1999**, *187* (1), 151–181. https://doi.org/10.1016/S0010-8545(99)90232-1.

(18) Sánchez-Delgado, R. A.; Navarro, M.; Pérez, H.; Urbina, J. A. Toward a Novel Metal-Based Chemotherapy

against Tropical Diseases. 2. Synthesis and Antimalarial Activity *in Vitro* and *in Vivo* of New Ruthenium− and Rhodium−Chloroquine Complexes. *Journal of Medicinal Chemistry* **1996**, *39* (5), 1095–1099. https://doi.org/10.1021/jm950729w.

(19) Rosenberg, L. S.; Schulman, S. G. Tautomerism of Singly Protonated Chloroquine and Quinacrine. *Journal of Pharmaceutical Sciences* **1978**, *67* (12), 1770–1772. https://doi.org/10.1002/jps.2600671239.

(20) Banci, L.; Bertini, I.; Luchinat, C.; Scozzafava, A. Nuclear Relaxation in the Magnetic Coupled System Cu2Co2SOD. Histidine-44 Is Detached upon Anion Binding. *Journal of the American Chemical Society* **1987**, *109* (8), 2328–2334. https://doi.org/10.1021/ja00242a014.

(21) Arnesano, F.; Banci, L.; Piccioli, M. NMR Structures of Paramagnetic Metalloproteins. *Quarterly Reviews of Biophysics* **2005**, *38* (2), 167–219. https://doi.org/10.1017/S0033583506004161.

(22) Wang, W.; Zhang, X.; Huang, D.; Zhu, H.; Chen, C.; Liu, Q. Quinolinium Trichloro(Quinoline)Zinc(II). *Acta Crystallographica Section E Structure Reports Online* **2001**, *57* (12), m561–m563. https://doi.org/10.1107/S1600536801018414.

(23) Toscano, P. J.; DiMauro, P. T.; Geremia, S.; Randaccio, L.; Zangrando, E. The Synthesis and Crystal Structure of [Cr(Acacen)Py2] [ZnCl3py]. *Inorganica Chimica Acta* **1994**, *217* (1–2), 195–199. https://doi.org/10.1016/0020-1693(93)03745-V.

(24) The aliphatic side chain at the exocyclic nitrogen was substituted by a methyl group for computational convenience (Figure 5).

(25) Liakos, D. G.; Neese, F. Improved Correlation Energy Extrapolation Schemes Based on Local Pair Natural Orbital Methods. *Journal of Physical Chemistry A* **2012**, *116* (19), 4801–4816. https://doi.org/10.1021/jp302096v.

(26) Riplinger, C.; Pinski, P.; Becker, U.; Valeev, E. F.; Neese, F. Sparse Maps—A Systematic Infrastructure for Reduced-Scaling Electronic Structure Methods. II. Linear Scaling Domain Based Pair Natural Orbital Coupled Cluster Theory. *The Journal of Chemical Physics* **2016**, *144* (2), 024109. https://doi.org/10.1063/1.4939030.

(27) Guo, Y.; Riplinger, C.; Becker, U.; Liakos, D. G.; Minenkov, Y.; Cavallo, L.; Neese, F. Communication: An Improved Linear Scaling Perturbative Triples Correction for the Domain Based Local Pair-Natural Orbital Based Singles and Doubles Coupled Cluster Method [DLPNO-CCSD(T)]. *The Journal of Chemical Physics* **2018**, *148* (1), 011101. https://doi.org/10.1063/1.5011798.

(28) Becke, A. D. Density-functional Thermochemistry. III. The Role of Exact Exchange. *The Journal of Chemical Physics* **1993**, *98* (7), 5648–5652. https://doi.org/10.1063/1.464913.

(29) Stephens, P. J.; Devlin, F. J.; Chabalowski, C. F.; Frisch, M. J. Ab Initio Calculation of Vibrational Absorption and Circular Dichroism Spectra Using Density Functional Force Fields. *The Journal of Physical Chemistry* **1994**, *98* (45), 11623–11627. https://doi.org/10.1021/j100096a001.

(30) Weigend, F.; Ahlrichs, R. Balanced Basis Sets of Split Valence, Triple Zeta Valence and Quadruple Zeta Valence Quality for H to Rn: Design and Assessment of Accuracy. *Physical Chemistry Chemical Physics* **2005**, *7* (18), 3297. https://doi.org/10.1039/b508541a.

(31) These calculations favor a penta-coordination over a tetra-coordination in the gas phase (Section 5 in SI).

(32) Amin, E. A.; Truhlar, D. G. Zn Coordination Chemistry: Development of Benchmark Suites for Geometries, Dipole Moments, and Bond Dissociation Energies and Their Use To Test and Validate Density Functionals and Molecular Orbital Theory. *Journal of Chemical Theory and Computation* **2008**, *4* (1), 75–85. https://doi.org/10.1021/ct700205n.

(33) Weaver, M. N.; Merz, K. M.; Ma, D.; Kim, H. J.; Gagliardi, L. Calculation of Heats of Formation for Zn Complexes: Comparison of Density Functional Theory, Second Order Perturbation Theory, Coupled-Cluster and Complete Active Space Methods. *Journal of Chemical Theory and Computation* **2013**, *9* (12), 5277–5285. https://doi.org/10.1021/ct400856g.

(34) Hoops, S. C.; Anderson, K. W.; Merz, K. M. Force Field Design for Metalloproteins. *Journal of the American Chemical Society* **1991**, *113* (22), 8262–8270. https://doi.org/10.1021/ja00022a010.

(35) Peters, M. B.; Yang, Y.; Wang, B.; Füsti-Molnár, L.; Weaver, M. N.; Merz, K. M. Structural Survey of Zinc-Containing Proteins and Development of the Zinc AMBER Force Field (ZAFF). *Journal of Chemical Theory and Computation* **2010**, *6* (9), 2935–2947. https://doi.org/10.1021/ct1002626.

(36) Yu, Z.; Li, P.; Merz, K. M. Extended Zinc AMBER Force Field (EZAFF). *Journal of Chemical Theory and Computation* **2018**, *14* (1), 242–254. https://doi.org/10.1021/acs.jctc.7b00773.

(37) Marzari, N.; Vanderbilt, D. Maximally Localized Generalized Wannier Functions for Composite Energy Bands. *Physical Review B* **1997**, *56* (20), 12847–12865. https://doi.org/10.1103/PhysRevB.56.12847.

(38) Pearson, R. G. Hard and Soft Acids and Bases. *Journal of the American Chemical Society* **1963**, *85* (22), 3533–3539. https://doi.org/10.1021/ja00905a001.

(39) The zinc coordination bond lengths are overestimated as in the AIMD-BLYP simulation of **CL2** (Table S4).

(40) Fatmi, M. Q.; Hofer, T. S.; Randolf, B. R.; Rode, B. M. Stability of Different Zinc(II)−Diamine Complexes in Aqueous Solution with Respect to Structure and Dynamics: A QM/MM MD Study. *The Journal of Physical Chemistry B* **2007**, *111* (1), 151–158. https://doi.org/10.1021/jp0654213.

(41) Kleifeld, O.; Frenkel, A.; Martin, J. M. L.; Sagi, I. Active Site Electronic Structure and Dynamics during Metalloenzyme Catalysis. *Nature Structural Biology* **2003**, *10* (2), 98–103. https://doi.org/10.1038/nsb889.

(42) Maret, W.; Li, Y. Coordination Dynamics of Zinc in Proteins. *Chemical Reviews* **2009**, *109* (10), 4682–4707. https://doi.org/10.1021/cr800556u.

(43) Zhao, Y.; Truhlar, D. G. A New Local Density Functional for Main-Group Thermochemistry, Transition Metal Bonding, Thermochemical Kinetics, and Noncovalent Interactions. *The Journal of Chemical Physics* **2006**, *125* (19), 194101. https://doi.org/10.1063/1.2370993.

(44) Stoychev, G. L.; Auer, A. A.; Izsák, R.; Neese, F. Self-Consistent Field Calculation of Nuclear Magnetic Resonance Chemical Shielding Constants Using Gauge-Including Atomic Orbitals and Approximate Two-Electron Integrals. *Journal of Chemical Theory and Computation* **2018**, *14* (2), 619–637. https://doi.org/10.1021/acs.jctc.7b01006.

(45) The H1' and C1' shifts are not compared here with experiment, because in the calculations a methyl group replaces the aliphatic part of CQ, adjacent to these atoms, profoundly modifying the chemical environment.

(46) Krężel, A.; Maret, W. The Biological Inorganic Chemistry of Zinc Ions. *Archives of Biochemistry and Biophysics* **2016**, *611*, 3–19. https://doi.org/10.1016/j.abb.2016.04.010.

(47) Rampal, N.; Wang, H.-W.; Biriukov, D.; Brady, A. B.; Neuefeind, J. C.; Předota, M.; Stack, A. G. Local Molecular Environment Drives Speciation and Reactivity of Ion Complexes in Concentrated Salt Solution. *Journal of Molecular Liquids* **2021**, *340*, 116898. https://doi.org/10.1016/j.molliq.2021.116898.

(48) Farrell, D.; Miranda, E. S.; Webb, H.; Georgi, N.; Crowley, P. B.; McIntosh, L. P.; Nielsen, J. E. Titration_DB: Storage and Analysis of NMR-Monitored Protein PH Titration Curves. *Proteins: Structure, Function, and Bioinformatics* **2010**, *78* (4), 843–857. https://doi.org/10.1002/prot.22611.

(49) Schuth, N.; Mebs, S.; Huwald, D.; Wrzolek, P.; Schwalbe, M.; Hemschemeier, A.; Haumann, M. Effective Intermediate-Spin Iron in O_2-Transporting Heme Proteins.

Proceedings of the National Academy of Sciences **2017**, *114* (32), 8556–8561. https://doi.org/10.1073/pnas.1706527114.

(50) Müller, O.; Nachtegaal, M.; Just, J.; Lützenkirchen-Hecht, D.; Frahm, R. Quick-EXAFS Setup at the SuperXAS Beamline for *in Situ* X-Ray Absorption Spectroscopy with 10 Ms Time Resolution. *Journal of Synchrotron Radiation* **2016**, *23* (1), 260–266. https://doi.org/10.1107/S1600577515018007.

(51) Petuker, A.; Mebs, S.; Schuth, N.; Gerschel, P.; Reback, M. L.; Mallick, B.; van Gastel, M.; Haumann, M.; Apfel, U.-P. Spontaneous Si–C Bond Cleavage in (Triphos ^{Si})-Nickel Complexes. *Dalton Transactions* **2017**, *46* (3), 907–917. https://doi.org/10.1039/C6DT04048A.

(52) Ankudinov, A. L.; Ravel, B.; Rehr, J. J.; Conradson, S. D. Real-Space Multiple-Scattering Calculation and Interpretation of x-Ray-Absorption near-Edge Structure. *Physical Review B* **1998**, *58* (12), 7565–7576. https://doi.org/10.1103/PhysRevB.58.7565.

(53) Mukerji, I.; Andrews, J. C.; DeRose, V. J.; Latimer, M. J.; Yachandra, V. K.; Sauer, K.; Klein, M. P. Orientation of the Oxygen-Evolving Manganese Complex in a Photosystem II Membrane Preparation: An X-Ray Absorption Spectroscopy Study. *Biochemistry* **1994**, *33* (32), 9712–9721. https://doi.org/10.1021/bi00198a042.

(54) Dau, H.; Liebisch, P.; Haumann, M. X-Ray Absorption Spectroscopy to Analyze Nuclear Geometry and Electronic Structure of Biological Metal Centers?Potential and Questions Examined with Special Focus on the Tetra-Nuclear Manganese Complex of Oxygenic Photosynthesis. *Analytical and Bioanalytical Chemistry* **2003**, *376* (5), 562–583. https://doi.org/10.1007/s00216-003-1982-2.

(55) van der Spoel, D.; Lindahl, E.; Hess, B.; Groenhof, G.; Mark, A. E.; Berendsen, H. J. C. GROMACS: Fast, Flexible, and Free. *Journal of Computational Chemistry* **2005**, *26* (16), 1701–1718. https://doi.org/10.1002/jcc.20291.

(56) Lin, I.-C.; Seitsonen, A. P.; Tavernelli, I.; Rothlisberger, U. Structure and Dynamics of Liquid Water from Ab Initio Molecular Dynamics—Comparison of BLYP, PBE, and RevPBE Density Functionals with and without van Der Waals Corrections. *Journal of Chemical Theory and Computation* **2012**, *8* (10), 3902–3910. https://doi.org/10.1021/ct3001848.

(57) Gillan, M. J.; Alfè, D.; Michaelides, A. Perspective: How Good Is DFT for Water? *Journal of Chemical Physics*. American Institute of Physics Inc. April 7, 2016. https://doi.org/10.1063/1.4944633.

(58) Marx, D.; Hutter, J. *Ab Initio Molecular Dynamics*; Cambridge University Press, 2009. https://doi.org/10.1017/CBO9780511609633.

(59) Troullier, N.; Martins, J. L. Efficient Pseudopotentials for Plane-Wave Calculations. *Physical Review B* **1991**, *43* (3), 1993–2006. https://doi.org/10.1103/PhysRevB.43.1993.

(60) Berendsen, H. J. C.; Postma, J. P. M.; van Gunsteren, W. F.; DiNola, A.; Haak, J. R. Molecular Dynamics with Coupling to an External Bath. *The Journal of Chemical Physics* **1984**, *81* (8), 3684–3690. https://doi.org/10.1063/1.448118.

(61) Nosé, S. A Unified Formulation of the Constant Temperature Molecular Dynamics Methods. *The Journal of Chemical Physics* **1984**, *81* (1), 511–519. https://doi.org/10.1063/1.447334.

(62) Hoover, W. G. Canonical Dynamics: Equilibrium Phase-Space Distributions. *Physical Review A* **1985**, *31* (3), 1695–1697. https://doi.org/10.1103/PhysRevA.31.1695.

(63) Liberatore, E.; Meli, R.; Rothlisberger, U. A Versatile Multiple Time Step Scheme for Efficient Ab Initio Molecular Dynamics Simulations. *Journal of Chemical Theory and Computation* **2018**, *14* (6), 2834–2842. https://doi.org/10.1021/acs.jctc.7b01189.

(64) CPMD Version 4.3, http://www.cpmd.org/, Copyright IBM Corp 1990–2019, Copyright MPI Für Festkörperforschung Stuttgart 1997–2001.

(65) Neese, F. The ORCA Program System. *WIREs Computational Molecular Science* **2012**, *2* (1), 73–78. https://doi.org/10.1002/wcms.81.

(66) Jensen, F. Segmented Contracted Basis Sets Optimized for Nuclear Magnetic Shielding. *Journal of Chemical Theory and Computation* **2015**, *11* (1), 132–138. https://doi.org/10.1021/ct5009526.

(67) Vahtras, O.; Almlöf, J.; Feyereisen, M. W. Integral Approximations for LCAO-SCF Calculations. *Chemical Physics Letters* **1993**, *213* (5–6), 514–518. https://doi.org/10.1016/0009-2614(93)89151-7.

(68) Weigend, F. Hartree–Fock Exchange Fitting Basis Sets for H to Rn. *Journal of Computational Chemistry* **2008**, *29* (2), 167–175. https://doi.org/10.1002/jcc.20702.

(69) Neese, F.; Wennmohs, F.; Hansen, A.; Becker, U. Efficient, Approximate and Parallel Hartree–Fock and Hybrid DFT Calculations. A 'Chain-of-Spheres' Algorithm for the Hartree–Fock Exchange. *Chemical Physics* **2009**, *356* (1–3), 98–109. https://doi.org/10.1016/j.chemphys.2008.10.036.

(70) Barone, V.; Cossi, M. Quantum Calculation of Molecular Energies and Energy Gradients in Solution by a Conductor Solvent Model. *The Journal of Physical Chemistry A* **1998**, *102* (11), 1995–2001. https://doi.org/10.1021/jp9716997.

(71) Rehr, J. J.; Mustre de Leon, J.; Zabinsky, S. I.; Albers, R. C. Theoretical X-Ray Absorption Fine Structure Standards. *Journal of the American Chemical Society* **1991**, *113* (14), 5135–5140. https://doi.org/10.1021/ja00014a001.

(72) Rehr, J. J.; Albers, R. C.; Zabinsky, S. I. High-Order Multiple-Scattering Calculations of x-Ray-Absorption Fine Structure. *Physical Review Letters* **1992**, *69* (23), 3397–3400. https://doi.org/10.1103/PhysRevLett.69.3397.

(73) Rehr, J. J.; Albers, R. C. Theoretical Approaches to X-Ray Absorption Fine Structure. *Reviews of Modern Physics* **2000**, *72* (3), 621–654. https://doi.org/10.1103/RevModPhys.72.621.

(74) Newville, M. Larch: An Analysis Package for XAFS and Related Spectroscopies. *Journal of Physics: Conference Series* **2013**, *430*, 012007. https://doi.org/10.1088/1742-6596/430/1/012007.

For Table of Contents Only